Long-Term Intracellular Tracking of Label-Free Nanoparticles in Live Cells and Tissues with Confocal Microscopy.

Muriel F. Gusta[1,2,3], Lena M. Ernst[2], Oscar H. Moriones[1], Jordi Piella[1], Marta Valeri[2], Neus G. Bastus[1,3*], Victor Puntes[1,2,3,4*]

[1]*Institut Català de Nanociència i Nanotecnologia (ICN2), Campus UAB, Bellaterra, Barcelona, Spain.*
[2]*Vall d'Hebron Institut of Research (VHIR), Barcelona, Spain.*
[3]*Networking Research Centre for Bioengineering, Biomaterials, and Nanomedicine (CIBER-BBN), Madrid, Spain.*
[4]*Institució Catalana de Recerca i Estudis Avançats (ICREA), Barcelona, Spain.*

*Author for correspondence: neus.bastus@icn2.cat, victor.puntes@vhir.org

Abstract

The label-free imaging of inorganic nanoparticles (NPs) using Confocal Laser Scanning Microscopy (CLSM) provides a powerful and versatile tool for studying interactions between NPs and biological systems. Without the need for exogenous labels or markers, it simply benefits from the differential scattering of visible photons between biomaterials and inorganic NPs. Validation experiments were conducted on fixed and living cells in real-time, as well as mouse tissue sections following parenteral administration of NPs. Additionally, by incorporating reporter fluorophores and utilizing both reflectance and fluorescence imaging modalities, the method enables high-resolution multiplex imaging of cellular structures and NPs. Different sizes and concentrations of Au NPs were tested as for Ag, Fe_3O_4, and CeO_2 NPs, all with biological interest. Overall, the comprehensive study of NP imaging by confocal microscopy in reflectance mode provides valuable insights and tools for researchers interested in monitoring the nano-bio interactions.

INTRODUCTION

Nanoparticles (NPs) have emerged as a powerful tool for monitoring and manipulating biological processes and states at the molecular level, making them a crucial emerging component in the fields of biology and medicine[1-8] for diagnosis and therapy.[9-15] Besides, the increasing use of NPs in industrial processes and commercial products highlights the need for extensive studies on nanosafety and nanotoxicity to ensure their safe application in human health and their fate in the environment. And yet, despite their enormous potential, our understanding of how NPs interact with cells and function in environmental sentinel species or inside the human body is still limited.

To better understand how NPs interact with biological systems, detailed long-term *in vitro* (cellular) and *in vivo* (tissue) studies are essential to determine their spatial and temporal distribution. Electron microscopy (EM) is still the primary technique for studying NPs at high spatial resolution in biological systems. Despite its relevance, it is costly, labor-intensive, limited to materials with sufficient electron density contrast, and mainly restricted to fixed specimens, which hinders real-time observations. Additionally, it cannot perform fluorescence imaging of biomolecules, and sub-cellular entities are identified solely based on electron density contrast. Consequently, membranes, nuclei, and organelles are revealed in a nonspecific manner. Oppositely, Confocal Laser Scanning Microscopy (CLSM) allows high spatial resolution imaging of fluorescence-labeled biomolecules in cells and tissues. However, while NPs display high electron density and contrast suitable for EM, NPs typically lack inherent fluorescence. Adding a fluorophore to their structure can interfere with their physicochemical properties and alter their composition and surface state, potentially impacting biological response.[16-23] Indeed, one of the main short-comings of fluorescence microscopy is a limited observation time imposed by photobleaching.

Alternatively, real-time optical microscopy techniques, such as scatter-enhanced phase-contrast microscopy,[24] hyperspectral stimulated Raman scattering microscopy,[25] optical diffraction tomography,[26] and reflected light hyperspectral microscopy,[27] or even X-ray microscopy[28] have been developed to track label-free NPs. However, these techniques are not standard techniques available to the broad scientific community and cannot simultaneously perform real-time imaging of label-free NPs and fluorescent biomolecules.

In this context, Rayleigh light scattering of NPs appears as an interesting available alternative.[29-31] This is the basis of Dark-field (DF) microscopy, which employs oblique illumination to enhance contrast in specimens that scatter the incoming light. It provide excellent means for monitoring NPs within cells, as their scattering signal remains stable over time. Since El-Sayed et al. demonstrated this capability in 2005,[32] novel approaches have further expanded the potential of DF microscopy.[33-36] Most of these studies rely on hardware custom modifications to

collect and process the scattered light on a dark field approach. Nevertheless, the light scattered by the NPs can be directly detected in a conventional CLSM working in reflectance mode at the wavelength of the illumination laser, representing an exciting alternative for directly visualizing NPs. Reflectance imaging mode utilizes contrast from variations in the refractive indices of sample constituents as far as their diffraction index differs from that of the biological matrix. We had employed this technique to track gold NPs interacting with different type of cells (Hela,[28] A431[37] and A549[38]), and Wang et al showed in 2019 the observation of label-free Ag NPs using a confocal fluorescence microscope.[39] Despite the potential of the technique, it is still relatively unexplored as far as we know.

By performing a systematic study of materials and biological matrices, we herein provide tools for understanding NPs imaging principles by confocal microscopy. The dual use of reflectance and fluorescence imaging modalities, combining NPs and reporter fluorophores, allows for long-term high-resolution multiplex imaging of cell structure and NPs in fixed and living cells. Importantly, the method has been successfully applied to complex biological samples, such as tissue sections, which require intricate sample processing and high-resolution imaging, to locate NPs after *in vivo* administration. Moreover, the method is extended to different materials relevant to the biomedical field, such as Ag, [40-44] Fe_3O_4 -nanomagnetite-,[6, 45, 46] CeO_2 -nanoceria-,[7, 47-51] and more complex Au@CeO_2 hybrid NPs. This approach enables real-time tracking of NP-cell interactions, providing valuable insights into the behavior and fate of NPs in biological systems.

The paper is divided into two sections. In section A, we use 100 nm gold nanoparticles (Au NPs) as a model NP to observe optimal parameters for the observation of its biodistribution and uptake in fixed and live cell cultures, and tissues after parenteral administration (see Supplementary Info **Scheme S1**). Au NP were chosen due to their well-known biocompatibility, optical properties, and available synthetic approaches that lead to highly monodisperse NPs with tuneable size and surface state. In section B, we study the conditions to observe different NPs and resolution limits. This structure allowed us for a focused exploration of specific aspects while also providing a more general understanding of NP imaging in biological systems.

RESULTS AND DISCUSSION

SECTION A.

Confocal Imaging of Au NPs in Biological Systems.

To determine the conditions to observe NPs in cells, citrate-stabilized Au NPs of ~100 nm were prepared following well-established protocols[52] and imaged using conventional CLSM in reflectance mode (**Fig. 1A**). Even if their size is below the optical resolution limit, scattering happens for few nm as far as there is a significant change in the refractive index that traveling photons experiment. Thus, by collecting the light scattered from NPs when irradiated with visible light, NPs can be observed.[28, 53] For this, samples were placed on a chambered 8-well cover-glass microslide. It is paramount to remark that in all these experiments, colloidal stable NPs have been used, meaning there was no aggregation (as DLS shows in **Table 1**), and obtained results can be ascribed to the optical response of individual Au NPs. The scattered light from the Au NPs is monochromatic, with the same wavelength as the employed laser. Samples were observed with a filter covering the laser wavelength range (±15 nm). Note that the scattering measured intensities dependent on the illumination wavelength, as experimentally revealed by the UV-Vis absorbance spectrum (**Fig. 1B**). Indeed, the scattering ability of NPs can be inferred from experimental data, but it cannot be directly determined from it. The UV-Vis absorbance spectrum, often referred to as the extinction spectrum, stands for the loss of light from a transmitted beam, and it is the sum of two contributions, absorption and scattering, that can be calculated but not independently measured. **Figure 1C** shows the calculated extinction (Qext), scattering (Qsca), and absorption (Qabs) coefficients based on the standard Mie theory. CLSM images of the scattered light of Au NPs at the four different lasers used are shown in **Figure 1D**. Independently of the laser of choice, discrete light spots can be clearly seen in all images. Thus, as the band of Au NPs extends from 400 to 600 nm, the light scattered from them can be detected at all available wavelengths. Even though the same settings were used for all the lasers, the measured signal intensities were significantly different (**Fig. 1E).** Obtained results show how the strongest scattering occurs when Au NPs are irradiated by the light within the maximum scattering, corresponding to a laser excitation of 561 even if longer wavelengths display higher albedo -the contribution of scattering to the total extinction- (**Fig. 1C, inset**), evidencing how the laser choice is a critical point for the optimal visualization of the NPs.

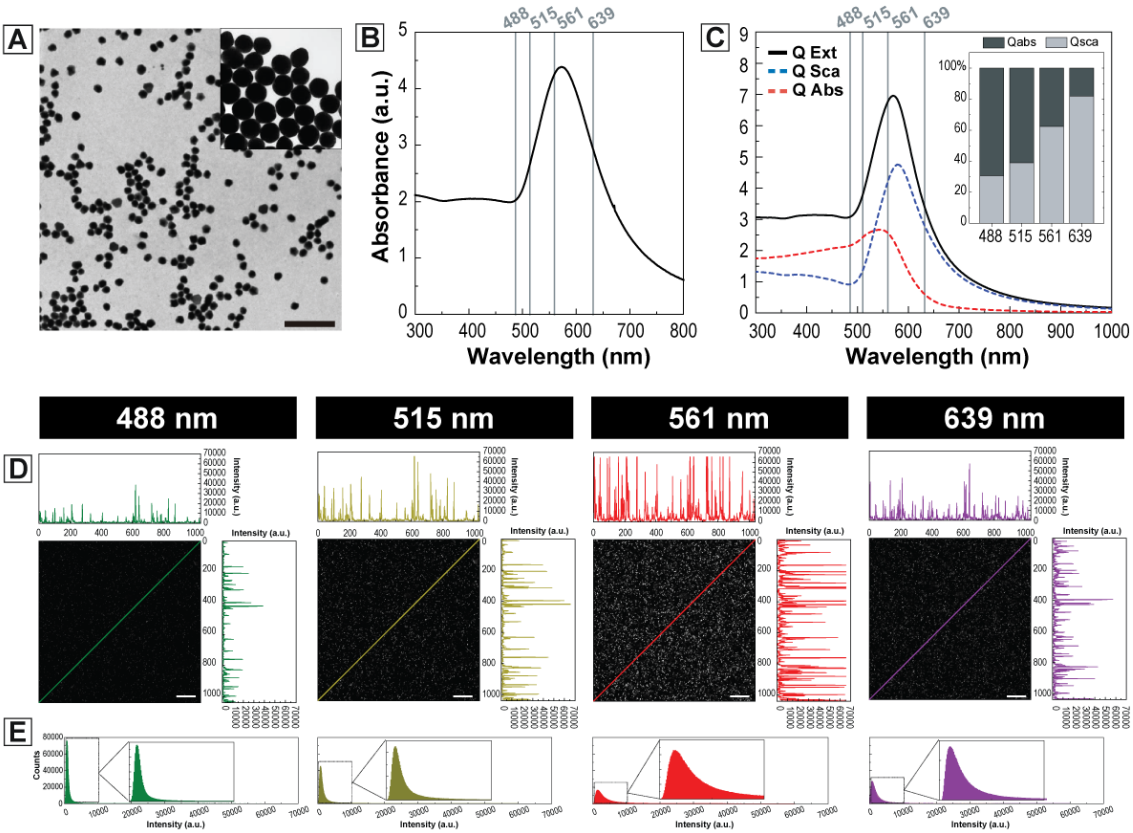

Figure 1. (A) Representative transmission electron microscopy (TEM) images of highly monodisperse citrate-stabilized Au NPs of ~100 nm. Scale bar = 500 nm. **(B)** Absorbance spectrum of Au NPs measured by UV–vis spectroscopy. Vertical lines correspond to confocal microscope excitation wavelengths (488, 514, 561, and 639 nm). **(C)** Calculated extinction (Qext), scattering (Qsca), and absorption (Qabs) efficiency of 100 nm Au NPs, **(C, inset)** and albedo -the ratio of scattering contribution to total extinction-. **(D)** CLSM images of the scattered light of Au NPs dispersed in sodium citrate 2.2. mM at the four different lasers used are shown. Scale bar = 10 µm. **(E)** Frequency (counts) analysis of the intensity profile, histogram from the measured intensities of Figure 1D plotting the number of events (Y axis) that a certain intensity was measured (X axis).

By combining fluorescence and reflectance imaging modalities, CLSM enables high-resolution multiplex imaging of both subcellular structures and NPs. This capability is particularly suitable for visualizing and locating NPs in fixed and living cells, and biological tissue sections after parenteral administration. To show this possibility, core-shell Au@SiO_2-FITC NPs were prepared, comprising an Au core (~60 nm) a, surrounded by an 80 nm concentric transparent SiO_2 shell (**Fig. S1**) containing a fluorophore (**Fig. 2A-C**). These NPs present dual-mode image capabilities providing, in a single entity, the fluorescent signal from the fluorophore and the scattering light from the Au NP allowing us to verify that the NP scattering signal and the fluorophore emission co-localize. The chosen fluorophore was the fluorescein isothiocyanate (FITC, excitation max. 490 nm, emission max. 525 nm). Additionally, by controlling the distance between the Au NP surface and the fluorophore location within the SiO_2 shell, the brightness of the organic fluorophore was increased up to 3.0 folds by virtue of the well-known phenomenon called Plasmon Enhanced Fluorescence.[54] Subsequently, HEK 293 cells were incubated with

Au@SiO_2-FITC NPs and imaged (**Fig. 2D**). This allowed us to simultaneously observe the distribution and localization of NPs relative to cellular structures. Before exposure to cultured cells, NPs were stabilized with Bovine Serum Albumin (BSA) to avoid NP aggregation when dispersed in the high-saline biological media.[55] After 24 hours, samples were fixed and stained for visualization. For each imaging, two lasers were used to irradiate the sample, and two corresponding bandpass filters were set to separate the scattered light from Au NPs and the fluorescence emission from FITC. Scattered light was detected under 561 nm laser excitation with an optical window filter set to 555-579 nm, while fluorescence was detected under 488 nm laser excitation and emission collected between 499-570 nm. Additionally, Phalloidin -excitation 639 nm, emission 650-694 nm- was used for F-actin cytoskeleton fibers staining (white), and Hoechst 3342 -excitation 405nm, emission 408-480nm- for nuclei staining (blue). Since the scattering of the Au core was acquired in a separated track, it is possible to image all the fluorescent markers in high resolution mode (see methods section) enabling for precise subcellular localization.

The spatial correlation between Au NPs and FITC signals proves that the light collected from the laser reflection comes precisely from the light emitted by the NP, confirming the reliability of NP scattering imaging in reflectance mode (**Table S1**). However, a relative fluorescence analysis from both channels (**Fig. S2**) reveals that there are more counts on the FITC channel, which could be attributed to the high number of dye molecules in each NPs, or eventually the presence of SiO_2-FITC NPs without Au core. This further emphasizes the importance and advantages of the label free imaging of NPs. On the other hand, the mean intensity from the Au scattering signal is higher than the FITC signal, which agrees with their relative cross-section values. Additionally, the staining of cellular organelles allows us to locate the NPs within the cell sample, either in the extracellular space, bound to the cell membrane, or intracellularly. Note that the signal from the scattering of the NP could be specifically collected without any signal overlap from the other emission tracks, nor did the presence of the NPs alter the emitted fluorescence proving the multiplexing capacity of the method (**Fig. S3**). Although with weaker intensities, NPs could be detected and localized with the other three available laser wavelengths (**Fig. S4**).

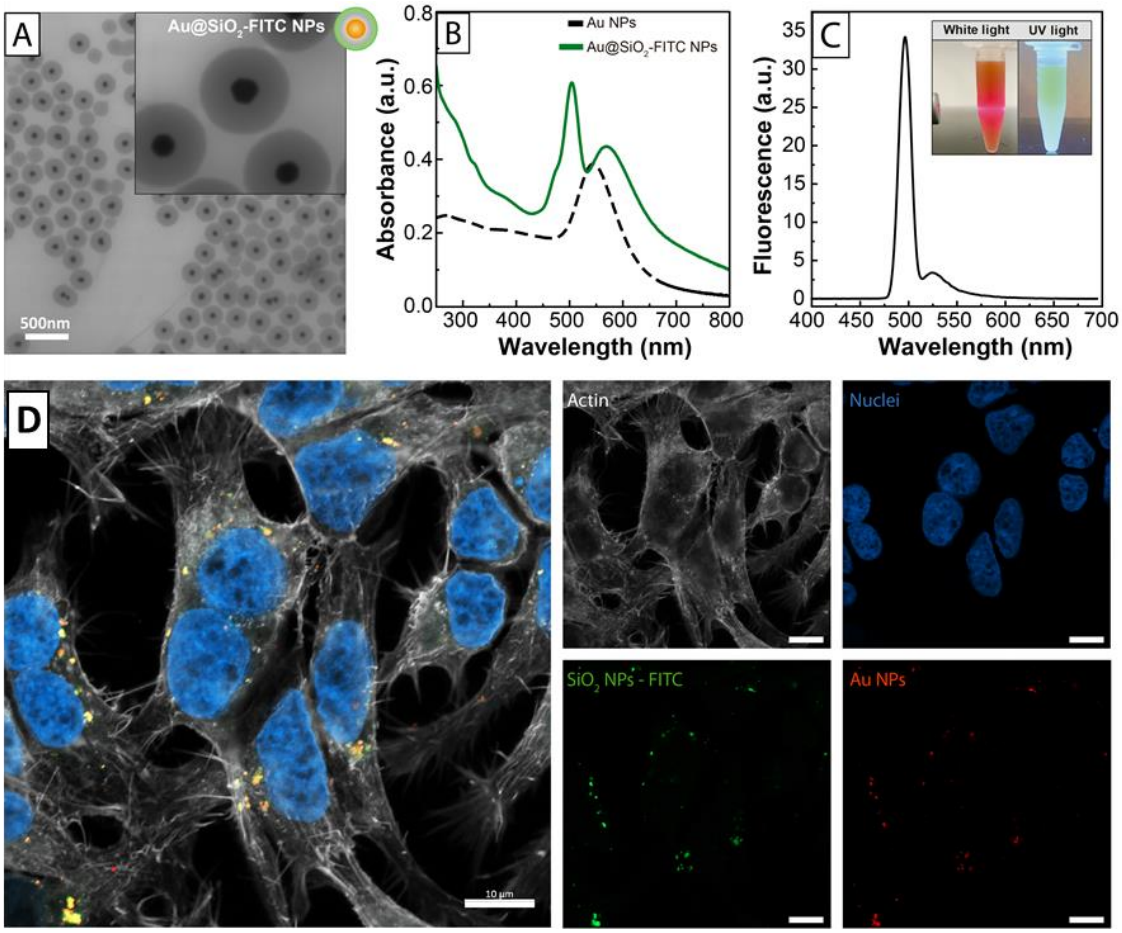

Figure 2. Imaging of Au@SiO_2-FITC NPs on HEK 293 cells. (A) Representative TEM images of Au@SiO_2-FITC NPs. **(B)** Absorbance spectrum of Au@SiO_2-FITC NPs measured by UV–vis spectroscopy. **(C)** Fluorescence spectra (emission) of colloidal solution of Au@SiO_2-FITC NPs. The spectra were taken in a 1:10 dilution in pure water at neutral pH and using an excitation wavelength of 495 nm. **(C, inset)** Pictures of the NPs taken upon exposure to white light and under ultra-violet excitation. **(D)** HEK 293 cells exposed to Au@SiO_2-FITC NPs. Composite image of the merged channel on the left, and split channels on the right showing stained actin (white) and nuclei (blue), and signal from NP imaged by fluorescence with FITC (green) and reflectance from the Au core (red). Scale bar = 10 µm.

One of the advantages of confocal microscopy is that it is possible to observe real-time interaction between NPs and live cells. Thus, NP-cell interactions in HEK 293 living cells were studied by passively monitoring the sample for 24 hours after ~100 nm Au NP exposure. **Figure 3** shows captions from the selected regions of Interest (ROIs) at different time points from the first 120 min after NP addition. A video of each one was mounted with all the acquired time frames (see SI). The nuclei and cytoplasm were stained before their observation. Two different signals coming from the Au NPs could be clearly observed, one "static", displayed as a single dot (arrows in **Fig. 3**), and the other "in movement", displayed as a short stripe. Static NPs correlate well in space with the cytoplasm marker or close to the nucleus, indicating that these NPs are in the intracellular space or bound to the cell membrane. Oppositely, NPs in the extracellular media are free to move, translating into a drift on their intensity signal which correlates to NP's Brownian motion in those

conditions. Note that the fact that the recording was set for 24 hours did not allow for high-resolution images as organic fluorophores would induce phototoxicity in cells when illuminated for such long periods.

Relative Fluorescence Intensity was measured from the Au signal imaged by reflectance mode (red) for all the time frames of ROI #1 and ROI #2. Results are summarized over time for both ROI in **Table S2**. Interestingly, spot signal counts increase with time, probably due to NPs sedimentation over time so that they appear in the focus plane. Accordingly, their percentage of area from the total image's pixels also increases proportionally. However, their mean signal intensity remains without significant differences, also in accordance with the fact that imaging NP by light scattering is not subjected to photobleaching.

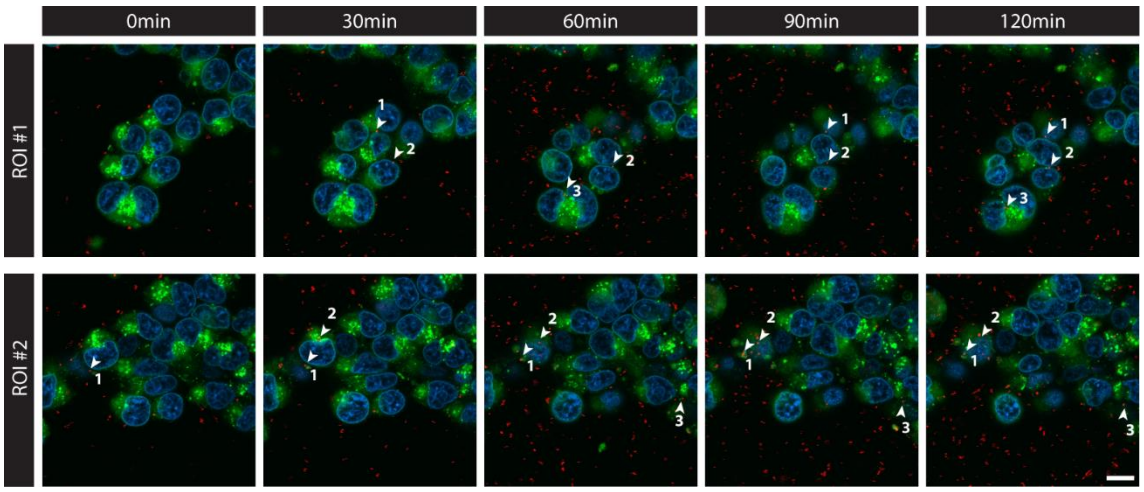

Figure 3. Time frames from the real-time imaging of Au NPs on HEK293 cells at time 0, 30, 60, 90, and 120 min. Cytoplasm (green) and nuclei (blue) staining were acquired by conventional fluorescence, and NPs (red) were imaged by reflectance. Numbers (1, 2, 3) pointed out with arrows (white) indicate NPs with the 'static' profile that can be followed along the time frames, suggesting their binding to the extracellular membrane or their internalization. Scale bar = 10 µm.

Imaging NPs through light scattering was further explored for its application in visualizing NPs in tissue sections after parenteral administration. For this, mice were injected intravenously with Au@SiO_2-FITC NPs and sacrificed 24 hours after administration. Tissue sections from the collected organs were stained (actin and nuclei). Images from the reconstructed complete tissue sections acquired in tiles with the wide-field fluorescence microscope are displayed in **Fig. S5** and **S6**. NPs were found to be well dispersed all over the organ samples. Representative areas from the tissue sections were selected and observed (**Fig. 4)**. In the liver section, NPs were mostly located outside the hepatocytes, in the sinusoidal space, and inside stellate cells. On the other hand, in the spleen samples, NPs were located in the margins of the white pulp. As in the cultured cells **(Fig.2)**, NPs were simultaneously imaged through the FITC signal by fluorescence mode

and NP scattering by reflectance mode. Both signals spatially correlate, proving NP light scattering on confocal microscopy is reliable for Au NPs imaging on biological entities, even in complex samples that underwent an intricate fixation and staining process for their CLSM visualization.

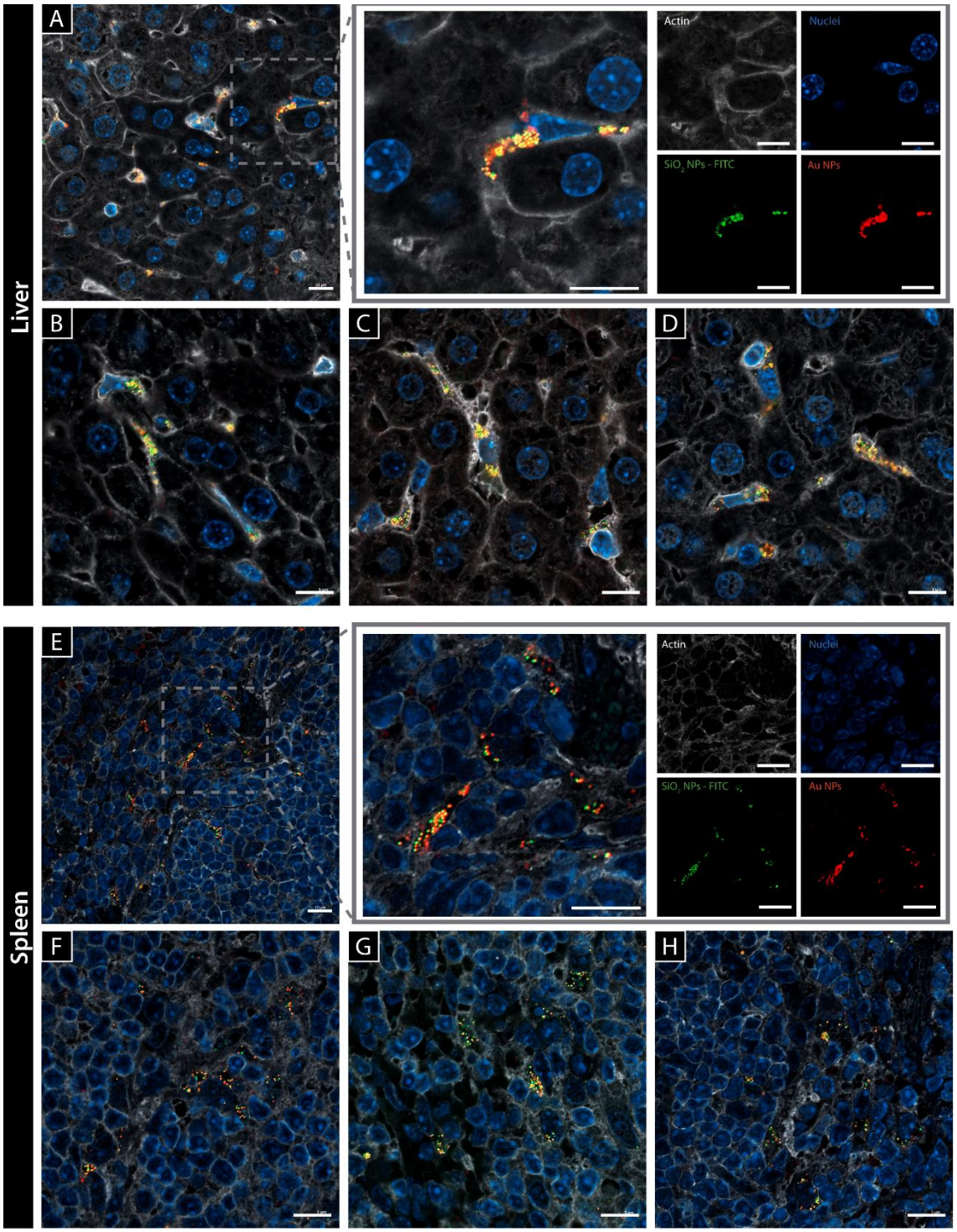

Figure 4. Representative CLSM images of NPs in tissue sections. Confocal imaging from the **liver (A-D)** and spleen **(E-H)** sections of the mouse exposed to Au@SiO_2-FITC NPs. A selected area is zoomed from a representative image from a liver **(A)** and spleen **(E)** section at 60X magnification. On the right, the

signal from each channel is split. Below, additional images from the liver **(B-D)** and spleen **(F-H)** sections at 40X magnification are shown. Scale bar = 10 μm.

SECTION B

Imaging other Sizes and Materials.

Light scattering is not limited to specific types or sizes of NPs, making it suitable for a wide range of NPs. In section B, the aim is to determine the capabilities and limitations of the imaging method in terms of its ability to resolve sizes and materials to allow investigate NP fate within biological systems.

Considering this, the Au NP's size resolution limits for confocal observation were experimentally studied. Unlike conventional dyes, the optical properties of NP are size-dependent. First, to study Au NP's size resolution limits, ~15 nm, ~50 nm, ~100 nm, and ~150 nm NPs were synthesized. TEM images are shown in **Figure 5A**, and the corresponding size distribution is summarized in **Table 1,** along with the DLS hydrodynamic diameter and the LSPR peak position measured by UV-Vis spectroscopy. These were imaged in colloidal suspension, using the reflectance mode at 561 nm. For this, 500μl of sample was placed on a chambered 8-well cover-glass microslide. Note that, here again, there is no aggregation throughout the experiment, as DLS showed, meaning that Au NPs are colloidally stable, and obtained results can be ascribed to the optical response of an ensemble of individual Au NPs (aggregation would alter dramatically their scattering properties). Acquired images are shown in **Figure 5B,** and measured intensities are plotted in **Figure 5C**. The individual contributions of absorption and scattering show how Au NPs with a diameter of 15 nm show negligible scattering (**Fig. 5D**). However, as size increases, the Au NP signal appears with a net contrast in the image. A complete size and wavelength-dependent study of the optical absorption, scattering, and efficiency of these Au NPs is shown in **Fig. S7**.

To further investigate this point, HEK 293 cells were exposed to ~15 nm, ~50 nm, and ~100 nm albuminized Au NPs (**Fig. S8**). Smaller Au NPs (~15 nm) only can be observed when accumulated (aggregated) in endosomes as normally happens after few hours after exposure to cells in culture for such NPs.[38] On the contrary, the light scattered by 50 nm and 100 nm, even when they are individually dispersed, is enough to be detected by CLSM.

Table 1. Characterization of the synthesized NPs.

	TEM (nm)	DLS diameter (nm)	LSPR (nm)	Mean Scattering Intensities	Sca Cross-section (cm^2/NP)
~15 nm	12.7 ± 1.4	16 ± 6	519	2.2 ± 0.4	3.0930×10^{-13}
~50 nm	53.8 ± 4.7	64 ± 12	535	21.5 ± 7.2	3.3336×10^{-10}
~100 nm	102.5 ± 8.9	114 ± 34	571	39.7 ± 13.9	1.16278×10^{-9}
~150 nm	148.4 ± 17.0	176 ± 51	546 / q653	52.9 ± 18.8	2.3770×10^{-9}

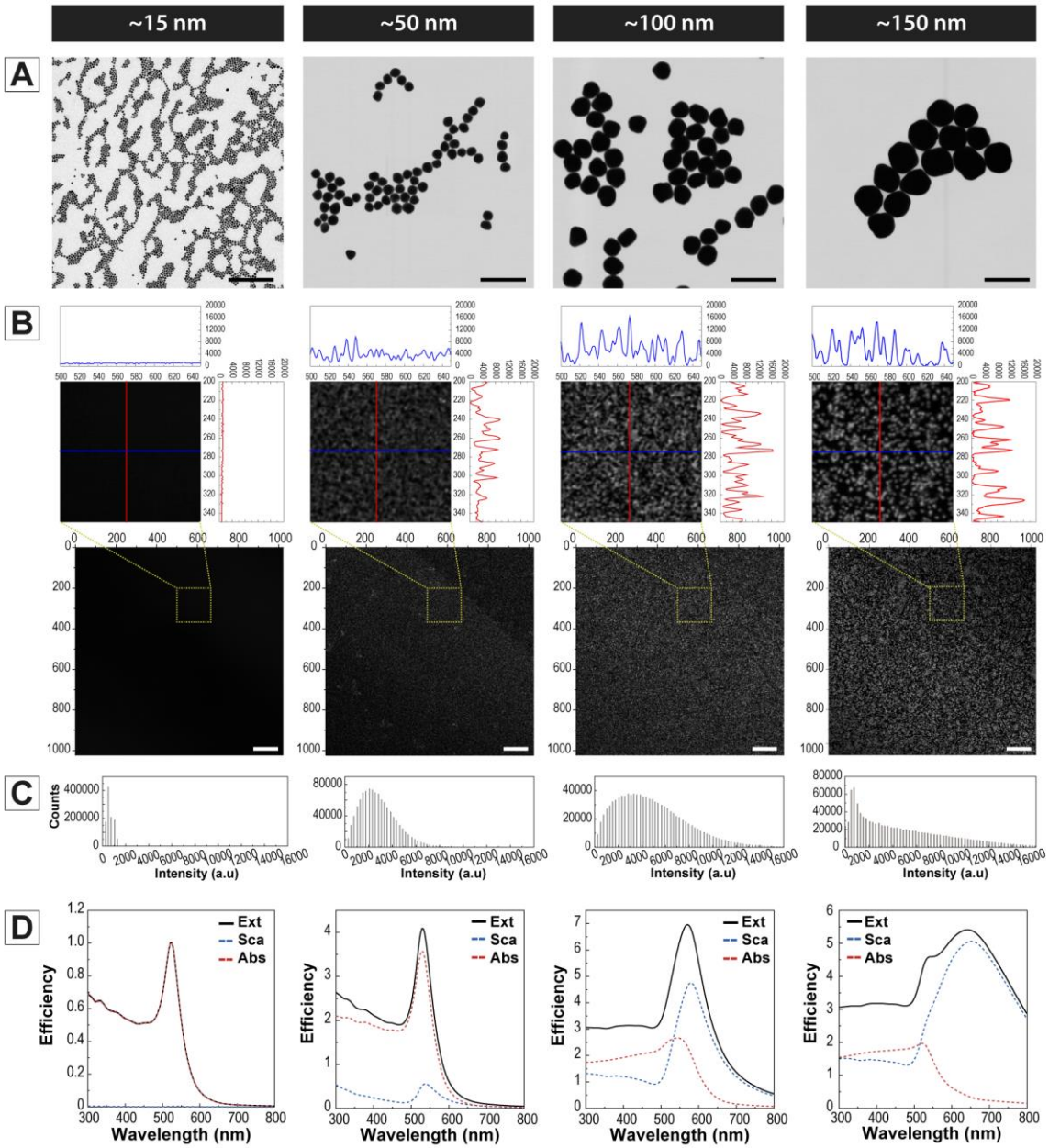

Figure 5. Au NP Size Resolution Limit. **(A)** Representative TEM images of highly monodisperse citrate-stabilized Au NPs of ~15 nm, ~50 nm, ~100 nm and ~150 nm. Scale bar = 250 nm. **(B)** CLSM images (Scale bar = 10 µm) and **(C)** intensity analysis of the scattered light of different-sized Au NPs at 561 nm. A selected region of interest is amplified to analyze the intensity profile. **(D)** Calculated extinction (Qext), scattering (Qsca), and absorption (Qabs) efficiency of ~15 nm, ~50 nm, ~100 nm and ~150 nm.

At this point, to make the study quantitative, a critical question is whether a single Au NP can be individually detected (the sample was prepared at very diluted conditions). Considering the experimental conditions when imaging at 100X magnification, the lateral resolution of the CLSM at 561 nm is R_L=160 nm, and the diffraction-limited spot size is 210 nm. As a consequence, if the distance of two adjacent spots containing Au NPs is larger than the lateral resolution, they can be distinguished in the *x*-*y* plane. A scan resolution of 1040×1040 pixels was used to acquire the CLSM images where each pixel size was around 82 nm. Having this consideration in mind, we measured the intensity of scattered light at the four different previously studied lasers of 8 selected spots that we consider individual ~100 nm Au NPs (**Fig 6A and Fig. S9),** and the mean intensity value was calculated (**Fig. 6B**). Measurements showed how scattered intensity depends on the employed laser. Notably, the results revealed that maximum intensity occurs at 561 nm and significantly lower at 639 nm, aligning with the SPR of a single 100 Au NPs at 571 nm. This distinctive laser-dependent profile strongly indicates that the measured scattered intensity originates from one individual NP. Conversely, aggregation is manifested through an increased absorption at longer wavelengths, potentially resulting in higher intensity values at the 639 nm wavelength.

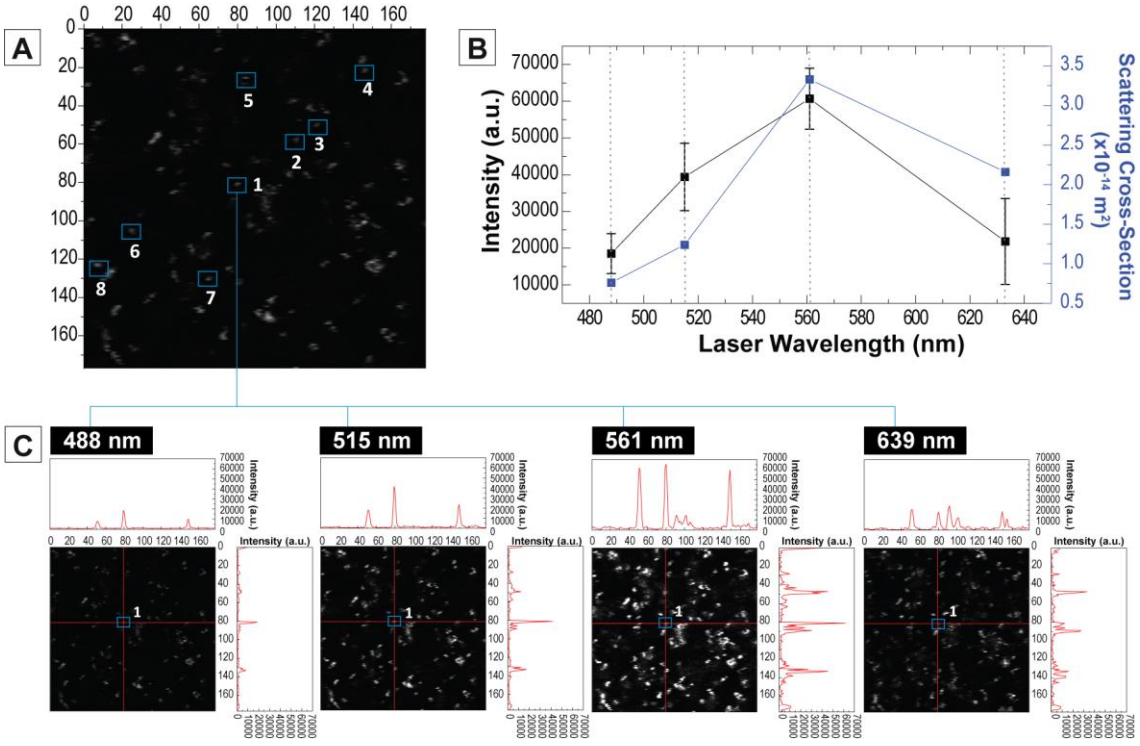

Figure 6. Detection of single Au NPs. (A) CLSM image of the scattered light of Au NPs and those selected for the study. CLSM image corresponds to pixels 0-166, 0-166 (x,y) of Figure 1. **(B)** Mean intensity values and calculated scattering cross-section values. The close correlation between the measured scattering intensity and the simulated scattering cross-section of ~100 nm Au NPs confirmed that the intensity profile provides information about a single NP event. **(C)** CLSM images of the scattered light of individual Au NPs (#1) at the four different lasers used. CLSM images of the scattered light of individual Au NPs from #2 to #8 are provided in the SI section **(Fig. S9)**.

The ability of NPs to scatter light can be applied to a variety of other NPs with different scattering profiles. To demonstrate this, silver NPs (Ag NPs),[56] cerium oxide NPs (CeO_2 NPs),[50] iron oxide (Fe_3O_4 NPs),[57] and gold-cerium hybrid core-shell NPs ($Au@CeO_2$ NPs)[58] were synthesized and fully characterized by TEM, DLS and UV-Vis spectra (**Table 2)**. Then, NPs were deposited on a cover-glass chambered microslide and imaged on the CLSM (**Fig. 7A** and **D**) at the wavelength at which their scattering contribution was highest. Discrete light spots could be clearly seen, regardless of the employed material. Notably, signal intensities correlated well with the experimentally measured absorbance (extinction) spectra (**Fig. 7B** and **E**) and relative calculated scattering efficiency (**Fig. 7C** and **F**) for each studied NP. Ag NPs exhibited a strong SPR band, with increased scattering intensity as NP size increased from 15 to 150 nm, with the highest scattering contribution at 100 nm. As a result, large Ag NPs were well observed while no significant signal was detected for the smallest Ag NPs (15 nm). Hybrid core-shell $Au@CeO_2$ NPs with two Au core sizes, 40 and 100nm, and corresponding CeO_2 shells of 8 and 18 nm, were also well visualized. Besides, in the case of oxides like CeO_2 and Fe_3O_4 NPs, the light scattered by individual NPs was too weak. Therefore, we employed synthesis recipes leading to discrete aggregates that can be observed. Plot profiles for each material based on CLSM images were performed, where the intensity profiles exhibit variations corresponding to their scattering efficiency (**Fig. S10**). These profiles serve as a reference to elucidate differences in efficiency across the depicted materials. Thus, results prove that NP of diverse materials with different scattering profiles can be observed on the CLSM. Indeed, if the scattering efficiency spectra of the NPs do not overlap, it would become possible to use distinct channels -laser wavelengths- to visualize each type of NP separately.

Table 2. Characterization of the synthesized NPs.

	TEM (nm)	DLS diameter (nm)	Peak Position (nm)
Ag	14.4 ± 2.1	18 ± 21	402
	43.2 ± 6.8	62.8 ± 22	429
	97.6 ± 9.6	101 ± 29	493 / q408
	140.8 ± 10.9	142 ± 54	544 / q425
CeO_2	4.2 ± 1.5	470 ± 2034	291
$Au@CeO_2$	Au 37.9 ± 3.8 CeO_2 shell 8.3±0.9	34 ± 7	283 / 546
	Au 103.9 ± 17.1 CeO_2 shell 18.4±4.3	179 ± 72	283 / 628
Fe_3O_4	10.7 ± 2.3	75 ± 14	-

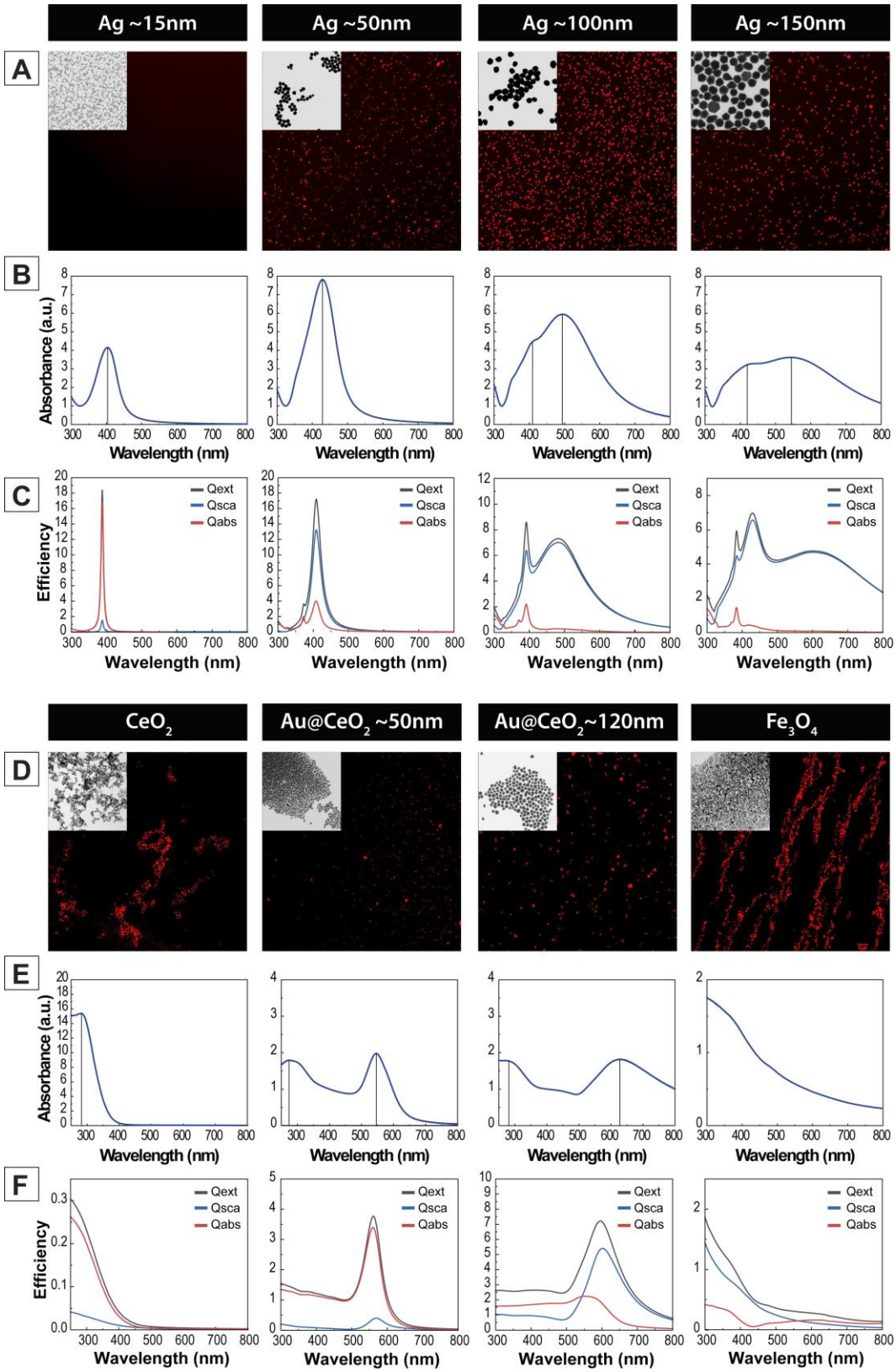

Figure 7. CLSM images of NPs of different sizes and compositions. (A, D) Ag NPs were imaged with the 515 nm laser, CeO_2 and Fe_3O_4 NPs with the 639 nm laser, and Au@CeO_2 NPs with the 561 nm laser. On the inset, representative TEM images. **(B, E)** Absorbance spectrum of NPs measured by UV–vis spectroscopy. **(C, F)** Calculated extinction (Qext), scattering (Qsca), and absorption (Qabs) efficiency.

CONCLUSIONS.

Imaging NP-scattered photons in reflectance mode provides a powerful and versatile imaging tool for studying the interactions between NPs and biological systems in real time. We show how the light scattered by NPs becomes the most direct label-free optical NPs detection method using a confocal microscope. It eliminates the need for exogenous labels or markers, relying on the detection of scattered photons from NPs. This label-free approach simplifies experimental procedures and allows for direct observation of NPs in their native state. CLSM imaging of various NP materials of biological interest, including Au NPs, Ag NPs, Fe_3O_4 NPs, and CeO_2 NPs in fixed cells, living cells, and tissue sections, demonstrates the broad applicability of CLSM for studying different NP systems and their interactions within biological systems. It is also important to stress that while organic fluorophores suffer from photoblinking and photobleaching, and working with them can induce phototoxicity when cells are illuminated for long periods, NP scattering requires much lower laser energies to be imaged in comparison to organic fluorophores, as scattering cross-section values can be several orders of magnitude higher than those of organic fluorophores (such as FITC) absorption cross-section, which is particularly important when observing living cells.

This technique offers a non-invasive and real-time imaging approach to investigate NP behavior and biological effects in living systems facilitating further understanding and development in the field. The comprehensive study of NP imaging by CLSM in reflectance mode provides valuable insights and tools for researchers who are interested in utilizing this method for their specific research needs.

ACKNOWLEDGEMENTS

We acknowledge financial support from the Spanish Ministerio de Ciencia, Innovación y Universidades (MCIU) (RTI2018-099965-B-I00, AEI/FEDER, UE) proyectos de I+D+i de programación conjunta internacional MCIN/AEI (CONCORD, PCI2019-103436) co-funded by the European Union and Generalitat de Catalunya (2021-SGR-00878). ICN2 is supported by the Severo Ochoa program from Spanish MINECO (SEV-2017-0706) and is funded by the CERCA Programme/Generalitat de Catalunya.

EXPERIMENTAL SECTION

Chemicals. Gold (III) chloride trihydrate ($HAuCl_4 \cdot 3H_2O$), silver nitrate ($AgNO_3$), trisodium citrate ($Na_3C_6H_5O_7$), tannic acid ($C_{76}H_{52}O_{46}$), Cerium (III) nitrate hexahydrate (99%), $Ce(NO_3)_3 \cdot 6H_2O$), iron (II) chloride ($FeCl_2$), iron (III) chloride ($FeCl_3$), tetramethylammonium hydroxide (TMAOH), tetraethyl orthosilicate (TEOS), fluorescein-5-isothiocyanate (FITC), (3-aminopropyl)triethoxysilane (APTES), and methacryloxypropyltrimethoxysilane (MPS), foetal bovine serum (FBS), bovine serum albumin (BSA), Sodium Phosphate Dibasic (Na_2HPO_4), Sodium phosphate monobasic (NaH_2PO_4), poly-L-lysine, phorbol 12-myristate 13-acetate (PMA), paraformaldehyde (PFA), Triton-X, and xylene were purchased from Sigma-Aldrich. Dulbecco's Modified Eagle Medium (DMEM), Hoechst 3342 (H1399), Prolong antifade mounting medium (11559306), goat anti-mouse Alexa Fluor568 (A110199), formalin and paraffin were purchased from ThermoFisher. Phalloidin Alexa Fluor 647 (ab176759), and Cell Tracking Red Dye Kit (ab269446) were purchased from Abcam. Anti-β-actin mouse monoclonal antibody (MAB8929) was purchased from R&D Systems.

All chemicals were used as received without further purification. Distilled water passed through a Millipore system (ρ = 18.2 MΩ) was used in all experiments. All glassware was first rinsed with Millipore water before use.

Gold Nanoparticle Synthesis. For this, 15, 50, 100, 150 nm Au NPs were synthesized using a well stablished seeded-growth method. It is based on the synthesis of small gold nanoparticles by citrate reduction of $HAuCl_4$, which are then used as templates to grow them by adding gold precursor up to the desired size.[52]

Silver Nanoparticle Synthesis. For this, 15, 50, 100, 150 nm Ag NPs were synthesized using a well stablished seeded-growth method. It is based on the synthesis of small silver nanoparticles by citrate and tannic acid reduction of $AgNO_3$, which are then used as seeds to grow them by adding gold precursor to the desired size. [56]

Cerium Oxide Nanoparticle Synthesis. CeO_2 NPs were synthesized by the chemical precipitation of cerium (III) nitrate hexahydrated in a basic aqueous solution, as reported previously by our group. Controlling the pH of synthesis, small-sized nanoceria can be obtained. Resulting CeO_2 NPs were then stabilized with TMAOH.[50]

Gold-Cerium Oxide Hybrid Nanoparticle Synthesis. Citrate-stabilized Au NPs of 40 nm and 100 nm were synthesized, following the method described above. The Au NPs were used without further purification as seeds for the CeO_2 coating, according to methods previously developed by our group.[58]

Iron Oxide Nanoparticle Synthesis. 7 nm Fe_3O_4 NPs were synthesized based on Massart's method. Amounts of $FeCl_2$ and $FeCl_3$ were dissolved in deoxygenated water to a molar ratio 1:2 and then added dropwise to a solution of deoxygenated TMAOH. After 30 min of vigorous stirring under a N_2 stream, the Fe_3O_4 precipitate was washed by soft magnetic decantation, redissolved in TMAOH at the desired concentration.[57]

Gold@Silica-FITC *Nanoparticle Synthesis*. First, citrate-stabilized 60 nm Au NPs of were synthesized, following the method described above. Later, the Au NPs were coated with a silica shell, used as a spacer, following the well reported the Stöber method by the hydrolysis and subsequent condensation of TEOS in ethanol under basic conditions. Then, the NPs were doped with the dye fluorescein-5-isothiocyanate (FITC) within the silica matrix, growing a second silica layer by adapting the method from Van Blaaderen.[59] Finally, a subsequent third silica shell for

protecting the doped dye from the environmental interactions, were done by another Stöber process. After this, the NPs were purified and dispersed in anhydride ethanol.

Calculations. Calculations of the extinction efficiency (Qext) of Ag and Au NPs of different diameters in water at 25 °C were obtained using MiePlot software and MultiLayer NP Simulator platform freely available online.[60, 61] The dielectric constant and refractive index of the metal were that provided by the programs while for the oxides the data were extracted from the literature.[62] The Qext was correlated with the empirical value of extinction, or absorbance, (A) through the Beer-Lambert law using the following equation:

$$A = \varepsilon\, c\, l \tag{1}$$

where ε is the extinction coefficient of the solution in units (M^{-1} cm^{-1}), c is the molar metal atom concentration and l (cm) is the path length of the beam of light through the solution. For particles of radi r (cm), the extinction coefficient can be expressed by:

$$\varepsilon = \frac{3\, V_m\, Q_{ext}}{4\ln(10) r} \tag{2}$$

Where Vm (M^{-1}) is the molar volume of the metal and Qext is the above defined dimensionless extinction efficiency.

$$Q_{ext} = \frac{extinction\ cross\ section}{cross\ section} = \frac{\sigma_{ext}}{\pi r^2} \tag{3}$$

Transmission Electron Microscopy (TEM). NPs were visualized using 80 keV TEM (Jeol 1010, Japan) and 20 keV STEM (FEI Magellan 400L XHR SEM). TEM grids were prepared as follows: 10 μL of sample were drop cast onto a copper TEM grid and left to dry in air. The TEM images acquired were used for the size distribution analysis. For each sample, the size of at least 500 particles was measured and the average size and standard deviation obtained.

Dynamic Light Scattering (DLS). A Malvern ZetaSizer Nano ZS instrument (Malvern Instruments) was used to measure NP size. An aliquot of the NP solution was placed in a cell and DLS analyses were performed. Measurements were conducted in a 1 cm optical path cell with precise control of temperature (25 °C).

UV-Vis Spectroscopy. The spectrum of each sample was recorded using Agilent Cary 60 UV-Vis Spectrophotometer (Agilent Technologies). An aliquot of the NP solution was placed in a cell and the analysis was performed in the 300−800 nm range at room temperature.

Confocal Laser Scanning Microscopy (CSLM). The Confocal Laser Scanning Microscope (Zeiss LSM980 with Airyscan 2 Super-resolution detector) was set to reflectance mode. For this, the dichroic mirror was retracted, only a T80/20 beam splitter was set instead, the reflection mode allowed, and the emission window was set at Δ15 nm to the laser source wavelength. Colours from the images acquired are chosen arbitrarily in each case to better discriminate all the signals collected.

Albuminization of Au NPs. A stock solution of Bovine Serum Albumin (BSA) was prepared at 10mg/ml in PB 10mM buffer. Au NPs were added onto the BSA solution to a final relative volume concentration 90-10%, and incubated overnight at 4ºC.

HEK-293 cells culture. HEK 293 cell culture was maintained in culture in 75 cm^2 tissue culture flask using DMEM with heat-inactivated foetal bovine serum (FBS) at 10% at 37 ºC and humidified 5% CO_2.

Confocal Imaging of NPs on fixed cultured cells. HEK 293 cell line (DSMZ) were seeded on a 8-well glass bottom microslide (Sarsted) at 100.000 cell/cm^2 and incubated overnight. Albuminized Au NPs of 15 nm ($2x10^{11}$ NP/ml), 50 nm ($2x10^{10}$ NP/ml) and 100 nm ($2x10^{9}$ NP/ml) and Au@SiO_2-FITC ($8.2x10^{9}$ NP/ml) NPs were added dropwise onto cell cultures and gently homogenized. At 24 hours cells were fixed with 4% PFA. For immunohistochemistry, samples were first permeabilized with Triton-X 0.2% - BSA 1% for 10min. Samples were incubated with Phalloidin Alexa Fluor 647 for 45min for actin staining. Nuclei were stained with Hoechst 3342 for 15 min. Fading was controlled using the Prolong antifade mounting medium.

Confocal Imaging of NPs on tissue sections. 200 µl of 1.5ug Au/ml of Au@SiO_2-FITC NPs ($2.7x10^{11}$ NP/ml) were intravenously injected to each mouse (n=2). At 24 hours, mice were sacrificed and liver and spleen were collected. The organs were briefly washed with normal saline, slightly dried with blotting paper and immersed for 4 hours in 4% formalin for tissue fixation. Next, tissues were embedded in paraffin following a standard protocol. For immunohistochemistry, paraffin-embedded samples were sectioned at 4µm using a microtome and transferred to a poly-lysine coated glass slide. The paraffin was then removed with xylene and the samples rehydrated. Samples were permeabilized with Triton-X 0.2% for 10min. Sections were incubated with anti-β-Actin mouse monoclonal antibody overnight at 4ºC, followed by an incubation with a secondary antibody goat anti-mouse Alexa Fluor-568. Nuclei were stained with Hoechst 3342. Fading was controlled using the Prolong antifade mounting medium.

Confocal Imaging of NPs on *in vivo* cultured cells. HEK-293 cell line were seeded on an 8-well glass bottom microslide (Sarsted) at 100.000 cell/cm^2 and incubated overnight. Cells were labelled with Cell Tracking Red Dye Kit for 2 hours, and nuclei were stained with Hoechst 3342 for 15 min. Samples were placed on the Confocal Microscope (37 ºC, 5% CO_2) and Albuminized 50 nm Au NPs ($2x10^{10}$ NP/ml) were added dropwise onto cell cultures and gently homogenized. At this point started the sample recording for 24 hours to monitor the interaction of cell-NP. For the first 4 hours, images were acquired every 15 min, and from that point forward, the acquisition was done every hour.

References

[1] P. Englebienne, A. V. Hoonacker, M. Verhas, *Spectroscopy* **2003,** *17*, 372913.
[2] R. A. Sperling, P. Rivera Gil, F. Zhang, M. Zanella, W. J. Parak, *Chemical Society Reviews* **2008,** *37* (9), 1896-1908.
[3] P. K. Jain, X. Huang, I. H. El-Sayed, M. A. El-Sayed, *Accounts of Chemical Research* **2008,** *41* (12), 1578-1586.
[4] H. Jans, Q. Huo, *Chemical Society Reviews* **2012,** *41* (7), 2849-2866.
[5] P. K. Jain, K. S. Lee, I. H. El-Sayed, M. A. El-Sayed, *The Journal of Physical Chemistry B* **2006,** *110* (14), 7238-7248.
[6] P. Reimer, T. Balzer, *Eur Radiol* **2003,** *13* (6), 1266-76.
[7] C. Xu, X. Qu, *NPG Asia Materials* **2014,** *6* (3), e90-e90.
[8] Q. A. Pankhurst, N. T. K. Thanh, S. K. Jones, J. Dobson, *Journal of Physics D: Applied Physics* **2009,** *42* (22), 224001.
[9] J. E. Talmadge, R. K. Singh, I. J. Fidler, A. Raz, *Am J Pathol* **2007,** *170* (3), 793-804.
[10] E. Casals, V. F. Puntes, *Nanomedicine (Lond)* **2012,** *7* (12), 1917-30.
[11] M. P. Monopoli, D. Walczyk, A. Campbell, G. Elia, I. Lynch, F. Baldelli Bombelli, K. A. Dawson, *Journal of the American Chemical Society* **2011,** *133* (8), 2525-2534.
[12] M. P. Monopoli, C. Aberg, A. Salvati, K. A. Dawson, *Nat Nanotechnol* **2012,** *7* (12), 779-86.
[13] S. Goy-López, J. Juárez, M. Alatorre-Meda, E. Casals, V. F. Puntes, P. Taboada, V. Mosquera, *Langmuir* **2012,** *28* (24), 9113-9126.
[14] E. Izak-Nau, M. Voetz, S. Eiden, A. Duschl, V. F. Puntes, *Particle and Fibre Toxicology* **2013,** *10* (1), 56.
[15] E. J. Cho, H. Holback, K. C. Liu, S. A. Abouelmagd, J. Park, Y. Yeo, *Molecular Pharmaceutics* **2013,** *10* (6), 2093-2110.
[16] M. M. van Schooneveld, D. P. Cormode, R. Koole, J. T. van Wijngaarden, C. Calcagno, T. Skajaa, J. Hilhorst, D. C. t Hart, Z. A. Fayad, W. J. Mulder, A. Meijerink, *Contrast Media Mol Imaging* **2010,** *5* (4), 231-6.
[17] C. Wu, B. Bull, C. Szymanski, K. Christensen, J. McNeill, *ACS Nano* **2008,** *2* (11), 2415-23.
[18] X. Michalet, F. Pinaud, T. D. Lacoste, M. Dahan, M. P. Bruchez, A. P. Alivisatos, S. Weiss, *Single Molecules* **2001,** *2* (4), 261-276.
[19] M. d. l. Á. Ramírez, Á. M. Martínez-Villacorta, V. Gómez-Vallejo, P. Andreozzi, G. Soler-Illia, J. Llop, S. E. Moya, *Nanoscale Advances* **2022,** *4* (9), 2098-2106.
[20] E. Bindini, M. d. l. A. Ramirez, X. Rios, U. Cossío, C. Simó, V. Gomez-Vallejo, G. Soler-Illia, J. Llop, S. E. Moya, *Small* **2021,** *17* (30), 2101519.
[21] W. Wang, K. Gaus, R. D. Tilley, J. J. Gooding, *Materials Horizons* **2019,** *6* (8), 1538-1547.
[22] N. M. S. Sirimuthu, C. D. Syme, J. M. Cooper, *Chemical Communications* **2011,** *47* (14), 4099-4101.
[23] J. Llop, P. Jiang, M. Marradi, V. Gómez-Vallejo, M. Echeverría, S. Yu, M. Puigivila, Z. Baz, B. Szczupak, C. Pérez-Campaña, Z. Mao, C. Gao, S. E. Moya, *J Mater Chem B* **2015,** *3* (30), 6293-6300.
[24] L. Tong, Y. Liu, B. D. Dolash, Y. Jung, M. N. Slipchenko, D. E. Bergstrom, J.-X. Cheng, *Nature Nanotechnology* **2012,** *7* (1), 56-61.
[25] B. Huang, S. Yan, L. Xiao, R. Ji, L. Yang, A. J. Miao, P. Wang, *Small* **2018,** *14* (10).

[26] D. Kim, N. Oh, K. Kim, S. Lee, C.-G. Pack, J.-H. Park, Y. Park, *Methods* **2018,** *136*, 160-167.
[27] S. Patskovsky, E. Bergeron, D. Rioux, M. Meunier, *J Biophotonics* **2015,** *8* (5), 401-7.
[28] S. Pujals, N. G. Bastús, E. Pereiro, C. López-Iglesias, V. F. Puntes, M. J. Kogan, E. Giralt, *Chembiochem* **2009,** *10* (6), 1025-31.
[29] N. G. Bastús, J. Piella, V. Puntes, *Langmuir* **2016,** *32* (1), 290-300.
[30] Y. Sun, Y. Xia, *Analyst* **2003,** *128* (6), 686-691.
[31] J. Piella, N. G. Bastús, V. Puntes, **2017,** *231* (1), 33-50.
[32] I. H. El-Sayed, X. Huang, M. A. El-Sayed, *Nano Letters* **2005,** *5* (5), 829-834.
[33] P. Zamora-Perez, D. Tsoutsi, R. Xu, P. Rivera_Gil. Hyperspectral-Enhanced Dark Field Microscopy for Single and Collective Nanoparticle Characterization in Biological Environments *Materials* [Online], **2018**.
[34] E. A. Gibbs-Flournoy, P. A. Bromberg, T. P. J. Hofer, J. M. Samet, R. M. Zucker, *Particle and Fibre Toxicology* **2011,** *8* (1), 2.
[35] K. Lindfors, T. Kalkbrenner, P. Stoller, V. Sandoghdar, *Physical Review Letters* **2004,** *93* (3), 037401.
[36] E. J. Guggenheim, A. Khan, J. Pike, L. Chang, I. Lynch, J. Z. Rappoport, *PLOS ONE* **2016,** *11* (10), e0159980.
[37] L. García-Fernández, J. Garcia-Pardo, O. Tort, I. Prior, M. Brust, E. Casals, J. Lorenzo, V. F. Puntes, *Nanoscale* **2017,** *9* (18), 6111-6121.
[38] J. Comenge, C. Sotelo, F. Romero, O. Gallego, A. Barnadas, T. G. Parada, F. Dominguez, V. F. Puntes, *PLoS One* **2012,** *7* (10), e47562.
[39] F. Wang, B. Chen, B. Yan, Y. Yin, L. Hu, Y. Liang, M. Song, G. Jiang, *Journal of the American Chemical Society* **2019,** *141* (36), 14043-14047.
[40] M. Yamanaka, K. Hara, J. Kudo, *Appl Environ Microbiol* **2005,** *71* (11), 7589-93.
[41] M. Palau, E. Muñoz, F. Gusta Muriel, N. Larrosa, X. Gomis, J. Gilabert, B. Almirante, V. Puntes, R. Texidó, J. Gavaldà, *Microbiology Spectrum* **2023,** *11* (3), e00280-23.
[42] H. H. Lara, N. V. Ayala-Núñez, L. d. C. Ixtepan Turrent, C. Rodríguez Padilla, *World Journal of Microbiology and Biotechnology* **2010,** *26* (4), 615-621.
[43] J. R. Morones, J. L. Elechiguerra, A. Camacho, K. Holt, J. B. Kouri, J. T. Ramírez, M. J. Yacaman, *Nanotechnology* **2005,** *16* (10), 2346-53.
[44] U. Klueh, V. Wagner, S. Kelly, A. Johnson, J. D. Bryers, *J Biomed Mater Res* **2000,** *53* (6), 621-31.
[45] K. Maier-Hauff, F. Ulrich, D. Nestler, H. Niehoff, P. Wust, B. Thiesen, H. Orawa, V. Budach, A. Jordan, *J Neurooncol* **2011,** *103* (2), 317-24.
[46] M. H. Schwenk, *Pharmacotherapy* **2010,** *30* (1), 70-9.
[47] J. Niu, A. Azfer, L. M. Rogers, X. Wang, P. E. Kolattukudy, *Cardiovasc Res* **2007,** *73* (3), 549-59.
[48] A. Asati, S. Santra, C. Kaittanis, J. M. Perez, *ACS Nano* **2010,** *4* (9), 5321-31.
[49] A. García, J. A. Cámara, A. M. Boullosa, M. F. Gustà, L. Mondragón, S. Schwartz, Jr., E. Casals, I. Abasolo, N. G. Bastús, V. Puntes, *Nanomaterials (Basel)* **2023,** *13* (15).
[50] D. Oró, T. Yudina, G. Fernández-Varo, E. Casals, V. Reichenbach, G. Casals, B. González de la Presa, S. Sandalinas, S. Carvajal, V. Puntes, W. Jiménez, *J Hepatol* **2016,** *64* (3), 691-8.
[51] E. Casals, M. Zeng, M. Parra-Robert, G. Fernández-Varo, M. Morales-Ruiz, W. Jiménez, V. Puntes, G. Casals, *Small* **2020,** *16* (20), e1907322.

[52] N. G. Bastús, J. Comenge, V. Puntes, *Langmuir* **2011,** *27* (17), 11098-11105.
[53] P. L. Truong, X. Ma, S. J. Sim, *Nanoscale* **2014,** *6* (4), 2307-2315.
[54] J.-F. Li, C.-Y. Li, R. F. Aroca, *Chemical Society Reviews* **2017,** *46* (13), 3962-3979.
[55] F. Barbero, L. Russo, M. Vitali, J. Piella, I. Salvo, M. L. Borrajo, M. Busquets-Fité, R. Grandori, N. G. Bastús, E. Casals, V. Puntes, *Seminars in Immunology* **2017,** *34*, 52-60.
[56] N. G. Bastús, F. Merkoçi, J. Piella, V. Puntes, *Chemistry of Materials* **2014,** *26* (9), 2836-2846.
[57] E. Casals, R. Barrena, A. García, E. González, L. Delgado, M. Busquets-Fité, X. Font, J. Arbiol, P. Glatzel, K. Kvashnina, A. Sánchez, V. Puntes, *Small* **2014,** *10* (14), 2801-2808.
[58] J. Piella, A. Gónzalez-Febles, J. Patarroyo, J. Arbiol, N. G. Bastús, V. Puntes, *Chemistry of Materials* **2019,** *31* (19), 7922-7932.
[59] A. Van Blaaderen, A. Vrij, *Langmuir* **1992,** *8* (12), 2921-2931.
[60] B. Tejerina, T. Takeshita, L. Ausman, G. C. Schatz, Nanosphere Optics Lab Field Simulator. **2008**.
[61] B. K. Juluri, J. Huang, L. Jensen, Extinction, Scattering and Absorption efficiencies of single and multilayer nanoparticles. **2010**.
[62] Y. Yin, Z.-Y. Li, Z. Zhong, B. Gates, Y. Xia, S. Venkateswaran, *Journal of Materials Chemistry* **2002,** *12* (3), 522-527.